Electrochemical Characterization of Polyelectrolyte/Gold Nanoparticle Multilayers Self-Assembled on Gold Electrodes

Mariana Chirea,*,† Vladimir García-Morales,‡ José A. Manzanares,‡ Carlos Pereira,† Rubin Gulaboski,† and Fernando Silva†

Departamento de Química da Faculdade de Ciências da Universidade do Porto, Rua do Campo Alegre 687, 4169-007 Porto, Portugal, and Departament de Termodinàmica, Universitat de València, E-46100 Burjassot, Spain

Received: July 9, 2005; In Final Form: September 21, 2005

Polyelectrolyte/gold nanoparticle multilayers composed of poly(L-lysine) (pLys) and mercaptosuccinic acid (MSA) stabilized gold nanoparticles (Au NPs) were built up using the electrostatic layer-by-layer self-assembly technique upon a gold electrode modified with a first layer of MSA. The assemblies were characterized using UV−vis absorption spectroscopy, cyclic and square-wave voltammetry, electrochemical impedance spectroscopy, and atomic force microscopy. Charge transport through the multilayer was studied experimentally as well as theoretically by using two different redox pairs $[Fe(CN)_6]^{3-/4-}$ and $[Ru(NH_3)_6]^{3+/2+}$. This paper reports a large sensitivity to the charge of the outermost layer for the permeability of these assemblies to the probe ions. With the former redox pair, dramatic changes in the impedance response were obtained for thin multilayers each time a new layer was deposited. In the latter case, the multilayer behaves as a conductor exhibiting a strikingly lower impedance response, the electric current being enhanced as more layers are added for Au NP terminated multilayers. These results are interpreted quite satisfactorily by means of a capillary membrane model that encompasses the wide variety of behaviors observed. It is concluded that nonlinear slow diffusion through defects (pinholes) in the multilayer is the governing mechanism for the $[Fe(CN)_6]^{3-/4-}$ species, whereas electron transfer through the Au NPs is the dominant mechanism in the case of the $[Ru(NH_3)_6]^{3+/2+}$ pair.

1. Introduction

Materials composed of two- and three-dimensional assemblies of nanoparticles (NPs) with narrow size distribution are becoming increasingly important in analytical and materials chemistry due to their practical applications in nanoelectronic and optoelectronic devices,[1,2] chemical sensors, biosensors, and catalysts.[3−7] Using the electrostatic and covalent interactions of bifunctional groups on the substrates, the assembly of individual NPs into three-dimensional structures has become an important and widespread research subject.[8,9] Au NPs-modified electrodes are usually fabricated by assembling Au NPs on electrode surfaces using organic linker molecules such as thiols and polymers.[10−12]

Tremendous efforts have been devoted to the characterization of nanoparticle arrays obtained by different assembling methods such as Langmuir−Blodgett,[13] polyelectrolyte,[14] or alkyl dithiol methods.[15,16] However, one of the most versatile and approachable ways to obtain three-dimensional nanostructured multilayers is the electrostatic layer-by-layer self-assembly technique, which was originally employed for polyelectrolyte multilayers (PEMUs).[17]

Although there are theoretical and experimental studies on charge and mass transport through PEMUs,[18−28] charge transport through multilayers composed of polyelectrolytes (PE) and NPs has not been carefully investigated and characterized yet at this somewhat early stage of interest in these systems.[29,30] Some previous works have reported a successful use of PE/NPs multilayers as electrochemical sensors[31] as well as their possible interest in designing junctions with rectifying properties.[32] Another previous work was focused on the characterization of PE/NPs assemblies in the optical domain.[33] These novel systems incorporate new and rich functionalities as well as other physical features, compared to PEMUs, such as electron transport through hopping or tunneling between neighboring NPs[29,34] or dynamic flocculation processes in the aggregation between NPs and the polyelectrolytes.[35] It is crucial for many applications, in any case, to ascertain the charge transport mechanisms taking place and to provide quantitative results on the physical properties ruling them as well as the means to control the permeability of PE/NPs multilayers.

In this work we describe the construction and characterization of structural and charge transport properties of electrostatically layer-by-layer self-assembled PE/NPs films composed of cationic poly (L-lysine) (pLys) and mercaptosuccinic acid (MSA) stabilized Au NPs with an average diameter of 2.5 nm (see Scheme 1 for the chemicals and Figure 1 for a scheme of the build-up process). We report here an extreme sensitivity to the charge of the last layer deposited, as well as to the charge of the nanoparticles, for the permeability of these assemblies to probe ions. This feature could make the assemblies studied highly attractive for applications ranging from water purification and desalination to ion sensing and protective reacting coatings for defense.[36] The assemblies were characterized using UV−vis absorption spectroscopy, cyclic and square-wave voltammetry, electrochemical impedance spectroscopy (EIS), and atomic force microscopy (AFM). Charge transport through the

* Corresponding author (telephone +351226082934; fax +35122608-2959; e-mail mariana.chirea@fc.up.pt).
† Universidade do Porto.
‡ Universitat de València.

10.1021/jp0537815 CCC: $30.25
Published on Web 10/25/2005

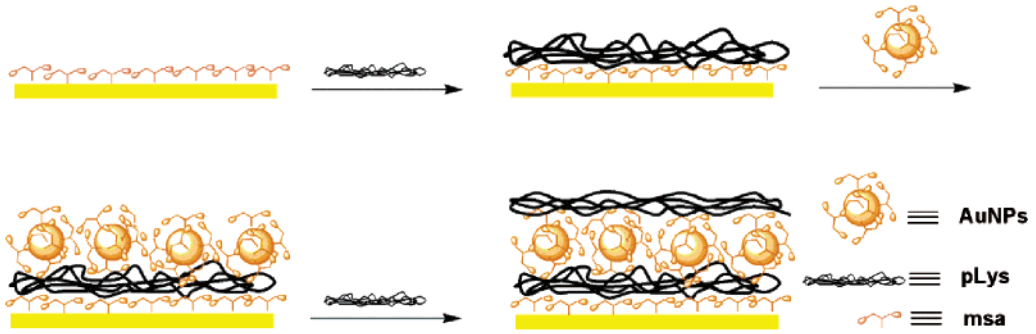

Figure 1. Scheme of the sequential self-assembly of the composite multilayer.

SCHEME 1: Chemical Structures of Mercaptosuccinic Acid (a), Poly(L-lysine) (b), and Gold Nanoparticles Stabilized with Mercaptosuccinic Acid (c)

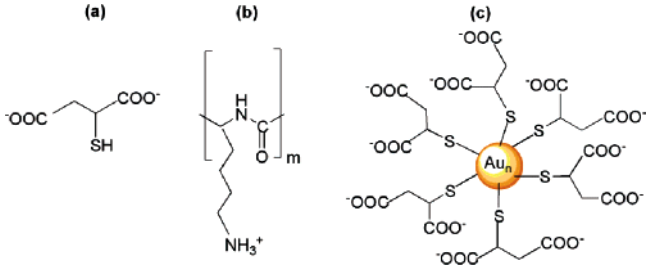

multilayer was studied experimentally as well as theoretically by using two different redox pairs $[Fe(CN)_6]^{3-/4-}$ and $[Ru(NH_3)_6]^{3+/2+}$. The theoretical model used is the capillary membrane model (CMM), which has been very recently developed to deal with charge transport through PEMUs,[27,28] and here its range of applicability is extended. Mass transport in this model accounts for the possible defects present in the multilayer leading to nonlinear diffusion.[37−43] There is substantial experimental evidence on the existence of defects and preferential paths for diffusion at the first stages in the growth of PEMUs.[44,45] We also demonstrate here the existence of defects in the early and intermediate stages of the build-up process of PE/Au NP multilayers by means of the AFM technique, thus supporting the validity of the CMM. The model provides excellent fittings to all impedance spectroscopy spectra, yielding information on the multilayer structure as well as the diffusion coefficients of the electroactive species within the multilayers.

2. Theory

The equivalent circuit in Figure 2 has been shown to account satisfactorily for the impedance spectra of several PEMUs, and it is also used here to analyze the PE/NP multilayers.[27,28] The solution resistance is R_s, the elements R_f and C_f represent the multilayer resistance and capacitance, respectively, and C_{dl} is the double-layer capacitance. The CMM[27,28] considers that the electrode coverage is not complete in the early stages of growth of the multilayer and describes it as an array of circular areas that are uncovered by both PE and NPs and, therefore, more accessible to the electroactive species.[37−43] These uncovered areas may persist during the sequential assembly of the multilayer, although they are progressively reduced in area and number as more layers are added. These areas play a key role in the transport properties of the multilayer, even after they are completely covered, because the film is less dense in those regions where there were opened spots previously and the flux density of the electroactive species is higher.

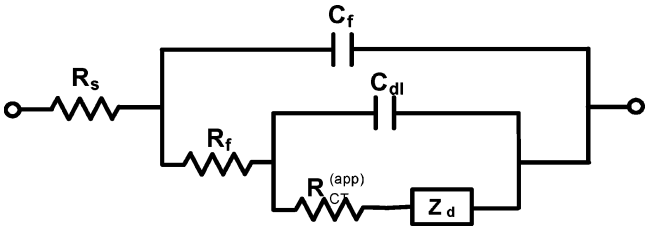

Figure 2. Equivalent circuit used for analyzing the impedance spectra.

As explained in detail elsewhere,[27,37−43] the diffusion impedance of partially blocked electrodes (used to fit our experimental results) is

$$Z_d^{(c)} = \sum_k \frac{\sigma_k^{(c)}}{\sqrt{\omega}}\left[1 + \frac{\theta}{(1-\theta)}\left(\frac{[1+(q_k/\omega)^2]^{1/2} + q_k/\omega}{1+(q_k/\omega)^2}\right)^{1/2} + j + \frac{j\theta}{(1-\theta)}\left(\frac{[1+(q_k/\omega)^2]^{1/2} - q_k/\omega}{1+(q_k/\omega)^2}\right)^{1/2}\right] \quad (1)$$

where

$$\sigma_k^{(c)} = \frac{RT}{n^2F^2A\sqrt{2D_k^f c_k^f}} \quad (2)$$

and

$$q_k = \frac{D_k^f}{r_a^2}\begin{cases} \dfrac{2}{\theta \ln(1 + 0.27/\sqrt{1-\theta})} & 1-\theta > 0.1 \\ 2.78 & 1-\theta \le 0.1 \end{cases} \quad (3)$$

In eqs 1−3, k is an index for the electroactive species ($k = 1$ for $[Fe(CN)_6]^{4-}$ and $Ru(NH_3)_6^{3+}$ and $k = 2$ for $[Fe(CN)_6]^{3-}$ and $Ru(NH_3)_6^{2+}$), R is the gas constant, T is the temperature, F is the Faraday constant, n is the number of electrons involved in the electrode reaction ($n = 1$ in our case), A is the electrode area, j is $\sqrt{-1}$, and ω is the angular frequency. The coverage θ, the radius r_a of a circular active area, and the radius r_b of inactive area surrounding the active site are related by the following equation:

$$1 - \theta = \frac{r_a^2}{r_b^2} \quad (4)$$

At high frequencies ($\omega/q \gg 1$) eq 1 becomes

$$Z_d^{(c)} \approx \sum_k \frac{\sigma_k^{(c)}}{(1-\theta)\sqrt{\omega}}(1+j) \quad (5)$$

and corresponds to a distribution of isolated electrodes where diffusion profiles do not overlap. The diffusion impedance reduces then to a Warburg element $\sigma_k^c/\sqrt{\omega}$ (planar semiinfinite diffusion) except for the factor $(1 - \theta)$ that accounts for the reduction in the electrode area.

At low frequencies ($\omega/q \ll 1$) eq 1 simplifies to

$$Z_d^{(c)} \approx \sum_k \frac{\sigma_k^{(c)}}{\sqrt{\omega}}\left[1 + \frac{\theta}{(1-\theta)}\sqrt{\frac{2\omega}{q}} + j\right] \qquad (6)$$

The real and imaginary parts are linear functions of $1/\sqrt{\omega}$. The diffusion profiles totally overlap and resemble semiinfinite diffusion. The term depending on the coverage in the real component of the diffusion impedance is characteristic of this situation and is usually referred to as *non-linear diffusion* resistance.[37−39]

At intermediate frequencies, the diffusion impedance does not vary linearly with $1/\sqrt{\omega}$ and eqs 5 and 6 cannot be used. The full eq 1 is needed then to account satisfactorily for the features of the diffusion profiles.

Due to the different nature of the paths as the coverage increases, the effective diffusion coefficient of species k in the multilayer, D_k^f, departs from that in the external solution, D_k^s, in a factor D_R, that is, $D_k^f \equiv D_R D_k^s$. For the sake of simplicity we take $D_1^s = D_2^s = D^s = 5.1 \times 10^{-6}$ and 1.8×10^{-6} cm^2 s^{-1} for the $[Fe(CN)_6]^{3-/4-}$ and $[Ru(NH_3)_6]^{3+/2+}$ species, respectively. These values for the diffusion coefficients have been calculated from the EIS spectra for the bare electrode.

Because pLys is a highly charged polyelectrolyte, partitioning effects need to be considered to provide a good account of the experimental observations. The partitioning is mainly electrostatic in nature (i.e., it is due to the Donnan equilibrium between the film and the external solution), although it also includes hydrophobic and steric effects. The ionic concentration of species k in the outer layer of the multilayer surface is given by $c_k^f = K_k c_k^s$, where c_k^s is its concentration in the bulk solution and K_k is the partition coefficient. For the sake of simplicity we take $K_1 = K_2 = K$. The apparent charge-transfer resistance is then evaluated as $R_{CT}^{(app)} = R_{CT}/K(1 - \theta)$, where the measured charge-transfer resistance R_{CT} for bare gold for the concentrations used was ca. 750 Ω for $[Fe(CN)_6]^{3-/4-}$ and 180 Ω for $[Ru(NH_3)_6]^{3+/2+}$.

The theoretical impedances for this equivalent circuit were calculated using Matlab. The solution resistance R_s and the double-layer capacitance C_{dl} were fixed to 300 Ω and 1.7 μF in all cases. The calculations were monitored by plotting the real and imaginary parts of the impedance as well as the diffusion impedance. It is important to stress that, because of the complexity of the elements involved, the calculations were done by tentatively approaching the experimental curves through appropriate choices of the parameter values. The fittings were then refined by evaluation of the squared sum of the distances between theoretical and experimental values. When this sum was found to be a minimum in the range considered and within a 95% confidence bound, we accepted the parameter values. The real and imaginary parts were also checked separately with the optimization toolbox of Matlab, yielding in all cases very good correlation coefficients in the range of 0.98−1.00.

3. Experimental Section

Chemicals. The following reagents were all used as received: hydrogen tetrachloroaurate(III) trihydrate ($HAuCl_4 \cdot 3H_2O$, 99.9%, Sigma Aldrich); mercaptosuccinic acid (HOOCCH$_2$CH(SH)COOH, 98%, Merck); poly(L-lysine) hydrobromide (pLys, MW 66700 g mol^{-1}, Sigma Aldrich); potassium dihydrogen phosphate (KH_2PO_4 pa quality, Merck); disodium hydrogen phosphate (Na_2HPO_4, pa quality, Merck); potassium hexacyanoferrate(III) (pa quality, Merck); potassium hexacyanoferrate(II) (pa quality, Merck); hexaammineruthenium(III) chloride (98%, Aldrich); methanol (99.8%, Sigma); $NaBH_4$ (>96%, Merck); $NaClO_4$ (pa quality, Merck); $NaNO_3$ (pa quality, Merck); $HClO_4$ (70%, redistilled, 99.999%, Aldrich); H_2SO_4 (pure, Pronalab); H_2O_2 30% (Fluka). Millipore filtered water (resistivity > 18 MΩ cm) was used to prepare all aqueous solutions and for rinsing. Before use, all of the glassware was cleaned with freshly prepared aqua regia (HNO_3/HCl = 1:3, %v), rinsed abundantly with Millipore water, and dried.

Nanoparticle Synthesis. Au NPs of about 2.5 nm diameter were synthesized following the Kimura method using 0.5 mmol of $HAuCl_4$ dissolved as a 5% (w/v) aqueous solution and 1 mmol of MSA in 100 mL of methanol in a 500 mL Erlenmeyer flask.[46] After 10 min of stirring, a freshly prepared 0.2 M aqueous sodium borohydride solution (25 mL) was added quickly under vigorous stirring. The yellow solution turned orange-brown immediately. Further addition of the reductant resulted in a flocculent brown precipitate. After 1 h of further stirring to complete the Au NPs formation, the solvent was decanted and the precipitate washed 5 times with a 20% (v/v) water/methanol solution by centrifugation (centrifuge Alresa-didacen II) at 4000 rpm, for 15 min each step, and sonication (Bandeline-Sonorex) to remove the inorganic (Na, Cl, B) or organic impurities. This process was further repeated twice with 99.8% methanol to remove unbound thiol or Au−MSA complexes. The precipitate obtained was suspended in ethanol and dried by rotary evaporation below 40 °C. The powder obtained was used to prepare the solution of Au NPs. Due to the pK_a^1 and pK_a^2 values of succinic acid, which are 4.19 and 5.64,[47] respectively, higher pH ensures the change of the carboxylic acid to its carboxylate ion form. The pH range of 5.0−6.0 coincides with the ionization range of the MSA bound to gold as established previously.[48] Also, the polymer has a pK_a value of 10. To ensure a good electrostatic interaction, the solutions were prepared in phosphate buffer solution (PBS), pH 6.

Transmission Electron Microscopy. The TEM images were obtained using a Tecnai G2 microscope operating at 120 kV with a point resolution of 0.5 nm. The samples were prepared by dropping the Au NPs aqueous solution on the copper−carbon grids followed by drying within a drybox for 24 h. The size distribution of the NPs was estimated using free software, Image J.

UV−Vis Spectroscopy. The UV−vis spectra of the samples were recorded on a Hitachi U-3000 spectrophotometer in the range of 200−800 nm. Quartz cuvettes with 1 cm light path and Au NPs solution 5 mg/10 mL were used for the optical characterization of the NPs. Multilayers were deposited on a silanized quartz slide. The quartz slide was placed perpendicular to the beam to maintain the same position during each measurement.

Gold Electrode Preparation. The gold electrodes were cleaned by repeated soaking in a 3:1 mixture of concentrated sulfuric acid and hydrogen peroxide (30%, piranha solution) for about 1 min, followed by thorough washing with large amounts of Millipore water. *Caution! Piranha solution is corrosive and reacts violently with organic materials.* Next, the electrodes were polished on microcloth pads (Buehler) using polycrystalline diamond suspensions of 1 and 0.25 μm, followed

by sonication in Millipore water for 30 min. Finally, the electrodes were cleaned electrochemically by cycling between the potentials −0.4 and 1.5 V versus Ag/AgCl in 0.02 M $HClO_4$ solution, at a scan rate of 100 mV/s until reproducible cyclic voltammograms for a clean gold electrode were obtained.

Multilayer Buildup. Freshly cleaned gold electrodes were immersed in a methanolic solution (10 mM) of MSA for 18 h, and then the carboxylate groups of the acid adsorbed on the surface were activated by immersion in basic solution (0.2 M NaOH) for 10 min, followed by washing with Millipore water. The modified electrodes were then immersed for 1 h in PBS of pLys (1 mg/mL). The positively charged polymer was the anchor for the electrostatic adsorption of the Au NPs negatively charged, for which the adsorption time was 6 h. The necessary time for the electrostatic adsorption of the Au NPs was determined by comparative study for different times of adsorption: 1, 3, 4, and 6 h, the last one being appropriate due to the features of the multilayered film, which was mechanically robust and stable during all of the measurements. The concentration of the Au NPs solution was 0.17 mg/mL. All adsorbate solutions were prepared freshly prior use. After every layer deposition, the electrodes were washed with Millipore water to remove unbound polymer or Au NPs. Alternating layers (Scheme 1) of cationic pLys and anionic Au NPs were deposited up to maximum $n = 7$ layers on the electrode surface. The number of layers deposited is limited by the electrode response.

The buildup of multilayers for the spectroscopic measurements was performed on quartz slides coated with 3-aminopropyltriethoxysilane (3APTS) proceeding as follows: first, the slides were immersed in 20% aqueous sulfuric acid, then washed with Millipore water, ethanol, and acetone, and immersed in anhydrous acetone for 2 h. Next, the substrates were placed in an appropriate container filled with 4% solution of 3APTS in anhydrous acetone and stored for 12 h at 50 °C. The anhydrous acetone was generated by storage over molecular sieves for 24−36 h. The 3APTS treatment coats the substrates with amino groups, which allows for the buildup of the multilayers by alternately exposing the slides to the solutions of negative Au NPs and positive pLys. After every layer deposition, the slide was washed with Millipore water and the UV−vis spectra were recorded between 200 and 800 nm.

Atomic Force Microscopy. AFM measurements were carried out with a Molecular Imagining PicoLe AFM using a silicon cantilever/tip (Nanosensors, cantilever resonance frequency of 65−90 kHz). The measurements were performed in tapping mode for every layer adsorbed on the substrate, and several scans were imaged over a given surface area to ascertain that there is no sample damage induced by the tip. The images were scanned in topography (Figure 5), amplitude, and phase mode (results not shown) with a resolution of 512 × 512 pixels. Au (111) slides (Arrandee), 11 mm diameter, were used as substrates, after cleaning with ethanol, acetone, and Millipore water, and dried under nitrogen. The AFM measurements were carried out twice and gave similar results. The electrostatic adsorption of the layers was achieved using freshly prepared solutions, each adsorption step being followed by washing with Millipore water and drying of the samples. The time of the electrostatic adsorption was the same as for the electrochemical measurements.

Cyclic Voltammetry. CV measurements were carried out with an Autolab PGSTAT 20 potentiostat (EcoChemie B.V., Utrecht, The Netherlands). A three-electrode cell with a gold electrode (Radiometer Analytical, 2 mm diameter) as working electrode, a platinum wire as counter electrode, and a Ag/AgCl (3 M KCl) as reference electrode (Metrohm) was used. The electrochemical cell was enclosed in a grounded Faraday cage, and the measurements were performed at room temperature (20 °C). For deaeration, nitrogen was purged in the solution about 15 min before each measurement was begun. Also, the cell was kept under flowing nitrogen during the experiments. CVs were measured between −0.2 and 0.6 V for the electrochemical probe $[Fe(CN)_6]^{3-/4-}$ and between −0.4 and 0.1 V for the electrochemical probe $[Ru(NH3)_6]^{3+/2+}$ at 50 mV s^{-1}.

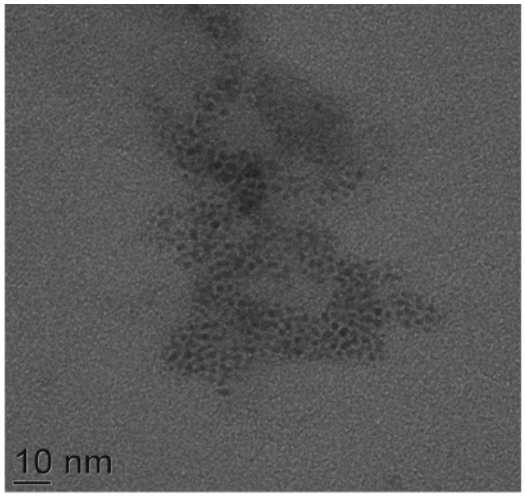

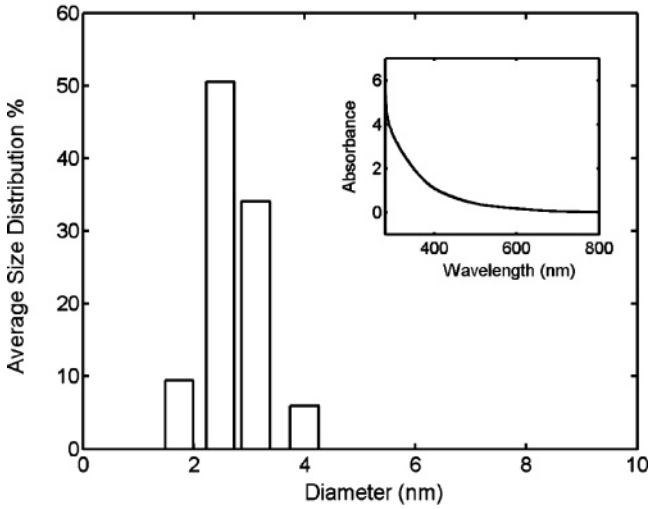

Figure 3. TEM image (top) and size distribution histogram (bottom) with the UV−vis spectrum (inset) of the Au NPs.

Square-Wave Voltammetry. Square-wave voltammograms were registered with an Autolab PGSTAT 20 potentiostat (EcoChemie B.V.) at 50 Hz, using a 50 mV amplitude and a 2 mV potential step.

Electrochemical Impedance Spectroscopy. Impedance spectra were recorded using a Frequency Response Analyzer Solartron (model 1250) connected to a Solartron potentiostat (model 1287). The frequency range was between 10000 and 0.5 Hz using an amplitude of 20 mV for a potential window around the midpeak potential determined from the CVs. All of the electrochemical measurements were repeated three times for both redox probes, and the reproducibility of the results was verified.

4. Results and Discussion

4.1. Characterization of the Au NPs. Figure 3 shows the TEM image (top), the size distribution histogram (bottom), and

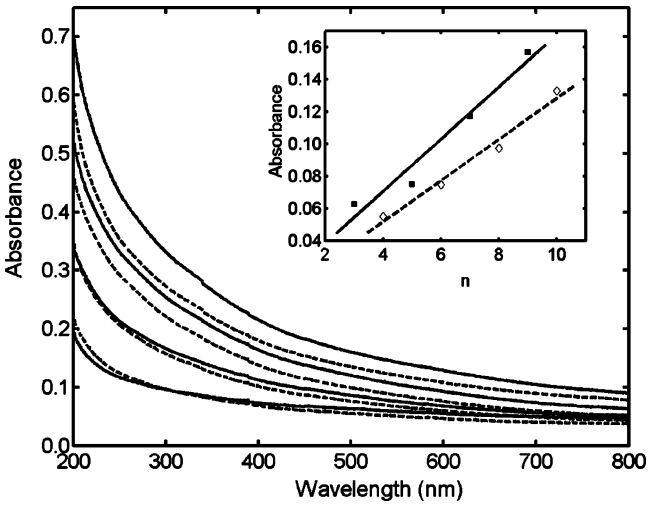

Figure 4. UV−vis spectra of the multilayers: solid lines for *n* odd (NPs terminated multilayers) and dashed lines for *n* even (pLys terminated multilayers) from bottom to top. (Inset) Absorbance at 510 nm.

the UV−vis spectrum (inset) of the NPs. Au NPs with an average diameter of 2.5 nm show no additional absorption peak around 500 nm. This is consistent with previous observations for AuNPs with a similar size[49−51] for which the surface plasmon band is essentially unidentifiable. The size distribution was evaluated by counting 320 NPs over a range of sizes between 1.7 and 4.2 nm with a standard deviation of ±0.30 nm. Because of the hydrogen-bonding interaction between the water molecules from the Au NPs solution and the carbonyl groups of the MSA on the Au NPs surface,[46] the distribution of the Au NPs in the TEM images is limited by the successive hydrogen-bonding networks. The water molecules act as "glue" connecting neighboring Au NPs, and this explains the appearance of the ensemble of Au NPs in the TEM images.

4.2. Multilayer Characterization. In the following discussion, *n* denotes the number of layers. For the electrochemical measurements the bare electrode corresponds to $n = 0$ and the first negatively charged, MSA, layer to $n = 1$. Then, even *n* corresponds to positively charged, pLys terminated multilayers. Odd *n* (≥ 3) corresponds to negatively charged Au NPs terminated multilayers.

UV−Vis Spectroscopy. Figure 4 shows the optical spectra of the films built on silanized quartz slide. No significant shift of the surface plasmon band is observed due to the reduced NP−NP distance, as previously noticed in the case of bigger NPs.[31] For either Au NP layers (solid lines) or pLys layers (dotted lines), the monotonic increase of absorbance with *n* demonstrates the systematic layering of the film. Au NP surface plasmon resonance is influenced by the refractive index of the surrounding environment. The pLys coating on the Au NP layers caused a decrease in the scattering of light, which leads to a decrease of absorbance values. The consecutive layering is also confirmed by the AFM images.

Atomic Force Microscopy. The surface morphology of the multilayers was investigated by AFM. Figure 5 shows AFM images of the MSA layer (a) and consecutively adsorbed layers of pLys (b, d, f) and Au NPs (c, e, g) as outermost layers assembled on the Au (111) slides. The scan size is 1 μm for all of the images. MSA chemisorbed on a clean slide (Figure 5a) has no visible effect in changing the topography of the substrate and exhibits a root-mean-squared (RMS) roughness of 2.8 nm, which is similar to that of the bare slide. The first pLys layer deposited on the modified gold surface (Figure 5b) appears to be homogeneously distributed and exhibits a slightly different topography. In the following steps of the build-up process two different topographies are observed: small spheroids (Au NPs) and an ordered structure formed by the backbone of the polymer (pLys). These structures are superimposed upon one another as more layers are deposited, thus indicating the complexation between the polymer and the Au NPs. The images of the film with one Au NPs layer on top of the first pLys layer (Figure 5c) exhibit a markedly different topography and a RMS roughness of 2.4 nm. This is fairly consistent with the mean particle size. As expected, here the spheroids dominate over the polymer−MSA background. The adsorption of the next pLys layer (Figure 5d) leads to an increased roughness (ca. 9.3 nm) and a pronounced change in the topography due to the large and ordered structure of the polymer. At this point, the pLys overcompensates the charge of the Au NPs. It is worth noting that a change appears in the topography when the next Au NP layer is deposited (Figure 5e), resulting in a compact spongelike structure with some black dots, circles, and darker areas (defects, pinholes, and potential preferential paths for diffusion). The next deposited pLys layer ($n = 6$, Figure 5f) looks similar to that of the multilayer with $n = 4$ but now the small spheroids appear more clearly, competing more with the polymer than in the previous case. Finally, when the next Au NPs layer is added (Figure 5g), both structural elements coalesce into homogeneous regions, and neither small spheroids nor ordered structures of the polymer are observed. At this point, the film has developed a dense, well-packed structure, very much in a manner observed previously in PEMUs[44,45] as well as in dendrimers/Ag NPs.[52] Wang et al.[53] have also observed in poly s-119/Au NPs multilayers a uniform coverage over areas macroscopic compared with the particle size when 20 bilayers have been deposited. We report here in addition the existence of pinholes and preferential paths in the earlier stages of the pLys/Au NPs multilayer growth.

4.3. Electrochemical Characterization Using $[Fe(CN)_6]^{3-/4-}$ as Electroactive Species. Figure 6 shows the CVs for the redox couple $[Fe(CN)_6]^{3-/4-}$. Multilayers with *n* odd exhibit an increased peak-to-peak separation and diminished peak currents (see Figure 6a), as could be expected because the outer layer and the electroactive ions are both negatively charged. The corresponding peak-to-peak separations are 0.093 V for $n = 0$ (bare gold), 0.192 V for $n = 1$ (MSA on gold), 0.290 V for $n = 3$ (first Au NPs layer), and 0.364 V for $n = 5$ (the second Au NPs layer). These CVs are similar to those observed in PEMUs.[18−28] As more layers are added, the peak current decreases and nonlinear slow diffusion begins to take place. A transition from peak-shaped to plateau-shaped voltammograms is then observed due to the increase of the charge-transfer resistance accompanying the gradual blocking of the electrode.

A somewhat different behavior is observed for *n* even (Figure 6b). The outer pLys layer has two important effects: (1) it leads to a rearranging of the multilayer, opening preferential paths for diffusion on the previous deposited NPs layers; and (2) it enhances the concentration of electroactive species within the film by means of Donnan inclusion. These two effects lead to quasi-reversible voltammograms with high peak currents. In this situation the peak-to-peak separations for each layer of pLys are slightly different compared with bare gold, being 0.077 V for $n = 2$, 0.106 V for $n = 4$, and 0.084 V for $n = 6$.

The effect of the outer layer can be more easily followed in the square-wave voltammetric responses recorded at a frequency of 50 Hz shown in Figure 7. In all cases, the presence of an outermost negatively charged layer, that is, the MSA layer or

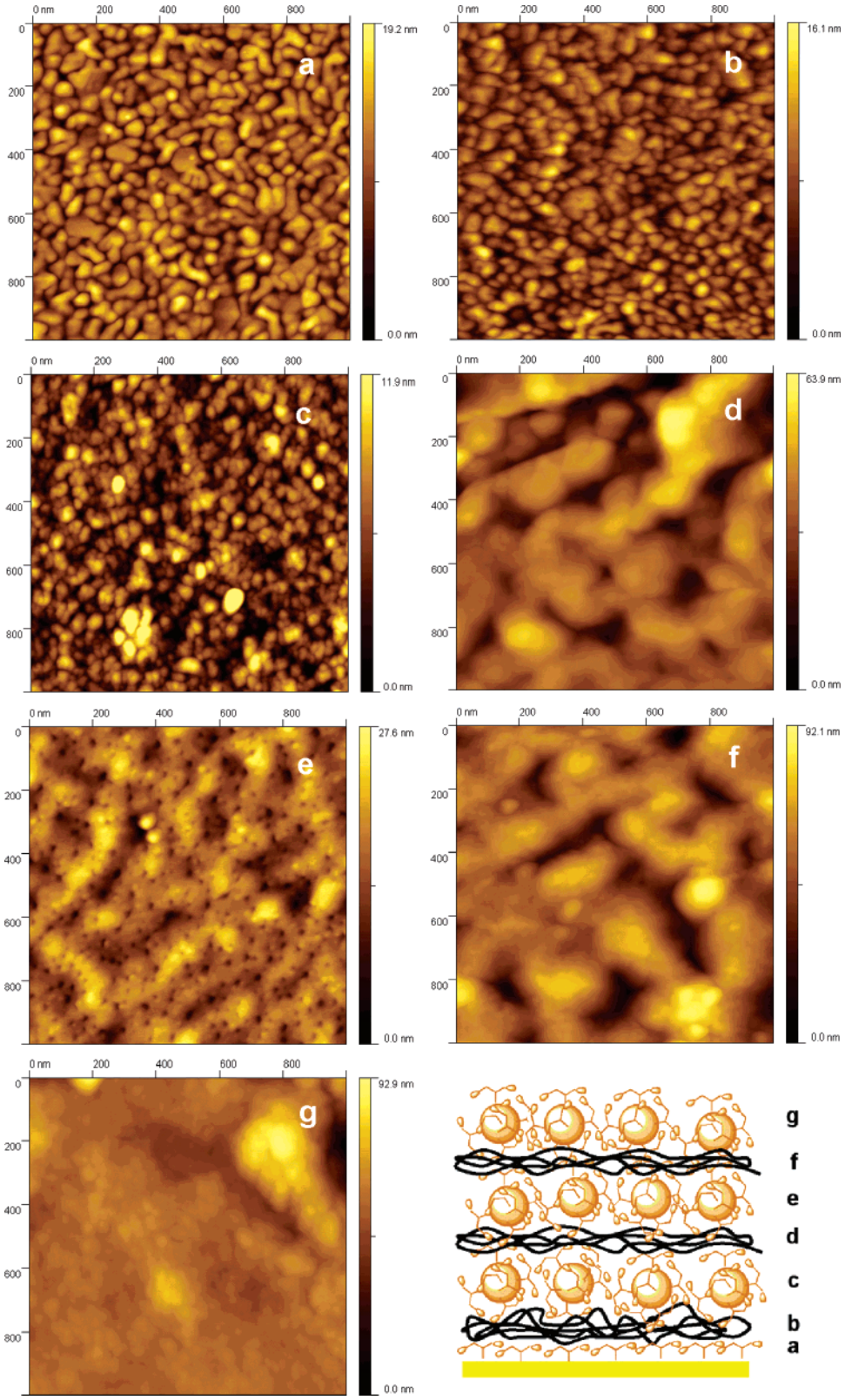

Figure 5. Topographic tapping mode AFM images at different stages of the multilayer buildup as indicated in the scheme. The scan size is 1 μm.

the anionic Au NPs layers (dashed lines), is portrayed by diminished forward and backward currents components of the square-wave voltammograms (denoted f and b) and by shifting of the square-wave peak potential in positive direction (i.e., the oxidation process is hindered and higher positive overpotential is required for its occurrence). This behavior is typical of systems with slow charge transfer.[54] In our system, the charge transfer is severely controlled by the deposited multilayer, which limits the active area of the electrode, slowing also the ion diffusion through the electrode surface. Contrarily, square-wave voltammograms with almost electrochemically reversible features are obtained when a pLys positively charged layer is the terminating one (continuous lines). The charge transfer is, therefore, strongly controlled by electrostatic interactions at the coated electrode|electrolyte interface, which decide the bulk behavior of the multilayer. This is strikingly seen in Figure 7d,

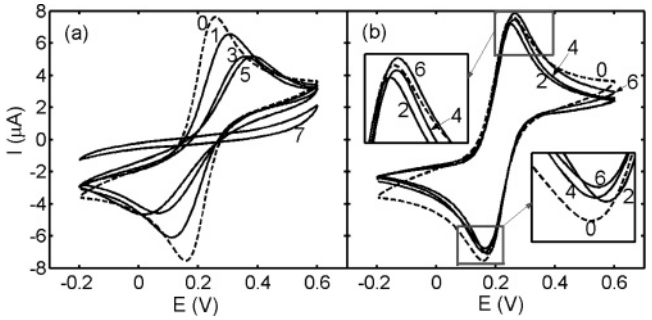

Figure 6. Cyclic voltammograms of the multilayer modified electrode in an aqueous 0.1 M $NaClO_4$ solution containing 1 mM $[Fe(CN)_6]^{3-}$ and 1 mM $[Fe(CN)_6]^{4-}$: (a) first MSA layer ($n = 1$) and NPs terminated multilayers with $n = 3$, 5, and 7 layers; (b) pLys terminated multilayers with $n = 2$, 4, and 6 layers. The bare electrode curve (dashed line, $n = 0$) is shown for comparison.

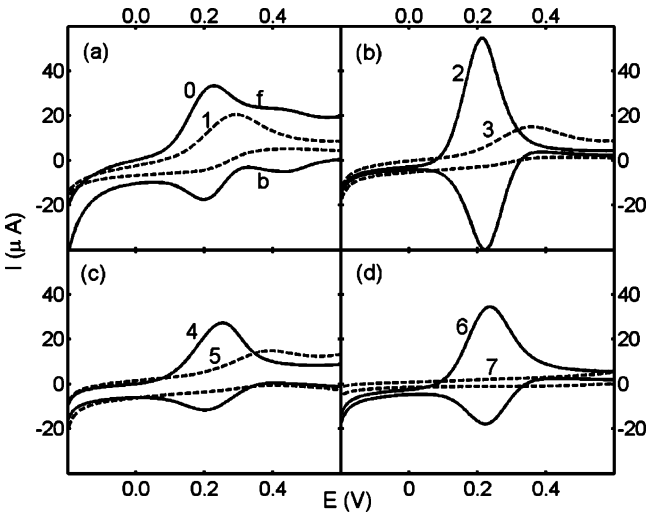

Figure 7. Square-wave voltammograms of the multilayer modified electrode in an aqueous 0.1 M $NaClO_4$ solution containing 1 mM $[Fe(CN)_6]^{3-}$ and 1 mM $[Fe(CN)_6]^{4-}$. Subscripts "f" and "b" stand for the forward and backward components of the current, respectively, and the starting potential was −0.2 V. The number of layers deposited is indicated in the figures.

where a complete diminishing of the voltammetric response when the third Au NPs layer is added to the multilayer is observed. This contrasts dramatically with the previous multilayer terminated in a third layer of pLys, which is permeable to the electroactive species.

The Nyquist plots at different stages of the multilayer buildup are shown in Figure 8. Theoretical curves obtained from the CMM for the parameter values given in Table 1 are also shown and agree excellently with the experimental results. The diffusion impedance is also plotted separately in Figure 8b to understand the effect of the pinholes in the impedance spectra.

In all cases where the self-assembled layers are terminating by Au NPs ($n = 3$, 5, and 7 in Figure 8) the Nyquist plots feature depressed semicircles that are mainly due to the combination of three time constants: the double-layer capacitance, C_{dl}, and the apparent charge-transfer resistance $R_{CT}^{(app)}$ at high frequencies, the film capacitance, C_f, and resistance, R_f, at intermediate frequencies, and the (nonlinear) diffusion Z_d at intermediate/low frequencies. Both the film resistance and the coverage θ increase with the number of layers as well as the film capacitance, indicating that the film area is increasing as well as the compactness of the multilayer. The decreasing value of both the diffusion coefficient in the film and the radius of the defects r_a (bare spots favoring the diffusion of the electroactive species to the electrode) is consistent also with the gradual attainment of a more compact structure and explains both the increasingly higher values of the impedance at low frequencies and the transition from peaked to plateau-shaped CVs.

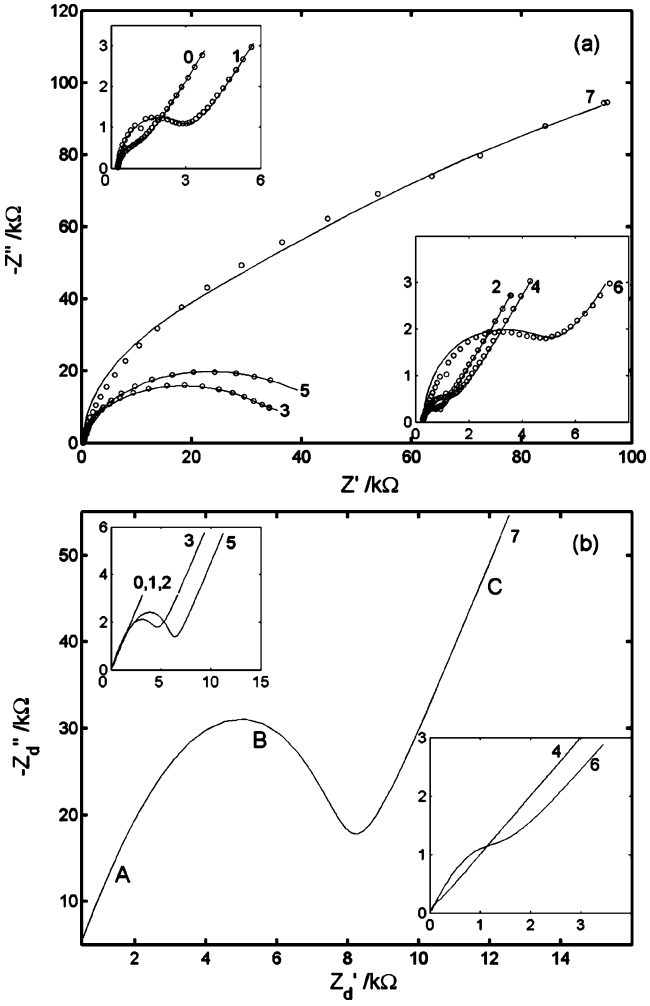

Figure 8. (a) Nyquist diagrams of the multilayer modified electrode in an aqueous 0.1 M $NaClO_4$ solution containing 1 mM $[Fe(CN)_6]^{3-}$ and 1 mM $[Fe(CN)_6]^{4-}$. The number of layers n is indicated close to the curves. The experimental data are represented by circles, and the solid lines have been calculated with the parameter values in Table 1. (b) Corresponding diffusion impedances Z_d calculated from eq 1.

TABLE 1: Parameter Values Used for Fitting the Impedance Data in Figure 8[a]

n	C_f (μF)	R_f (kΩ)	θ	r_a (μm)	D_R
0	0.250 ± 0.006				1.00 ± 0.01
1	0.60 ± 0.01	1.85 ± 0.04			0.91 ± 0.01
		pLys Terminated Multilayers			
2	0.60 ± 0.01	0.10 ± 0.01			0.79 ± 0.01
4	0.61 ± 0.01	0.55 ± 0.01	0.010 ± 0.002	11 ± 1	0.65 ± 0.01
6	0.82 ± 0.02	2.65 ± 0.04	0.40 ± 0.01	10 ± 1	0.72 ± 0.01
		Au NPs Terminated Multilayers			
3	0.60 ± 0.01	26.0 ± 0.3	0.80 ± 0.02	1.7 ± 0.1	0.27 ± 0.01
5	0.80 ± 0.01	27.0 ± 0.3	0.915 ± 0.009	0.71 ± 0.09	0.27 ± 0.01
7	0.81 ± 0.01	85 ± 1	0.915 ± 0.009	0.10 ± 0.01	0.0031 ± 0.0001

[a] Values are given for the 95% confidence bounds of the parameters. The partition coefficient K is 1.23 for pLys terminated multilayers and unity in other cases.

The parameter values for pLys terminated multilayers follow the same trend, although the values of R_f, C_f, and θ are lower than for Au NPs terminated multilayers. This indicates that the last pLys layer favors ion transport through the multilayers both by opening preferential paths for diffusion within the previous

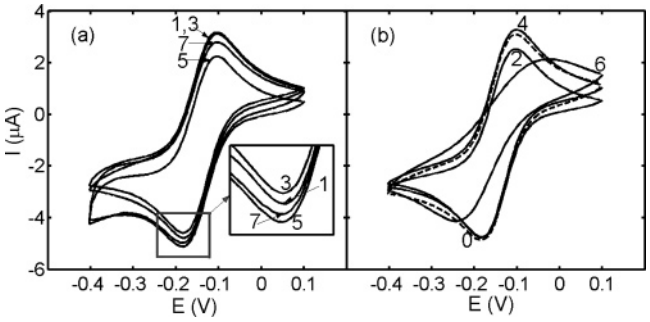

Figure 9. Cyclic voltammograms of the multilayer modified electrode in an aqueous 0.1 M $NaNO_3$ solution containing 1 mM $[Ru(NH_3)_6]^{3+}$ for different numbers of layers *n*.

layer of NPs (lower θ and C_f) and by overcompensating the negative charge of the outer layers of NPs, thus lowering R_f. This behavior was also observed in pLys/poly(styrene sulfonate) multilayers,[27] but an important difference must be mentioned here: the oscillation in R_f accompanying the addition of a new layer is 1 order of magnitude higher in pLys/Au NPs multilayers than in those PEMUs (compare, e.g., the R_f values in Table 1 with those in Table 2 of ref 27). This oscillation opens a potential route for developing extremely permselective membranes. The most important change takes place in passing from $n = 6$ to $n = 7$ layers. Both the radius of the pinholes and the diffusion coefficient in the film strongly decrease (the diffusion coefficient falls by 2 orders of magnitude), thus causing a large change in impedance. Almost a complete blocking in a more compact structure is achieved, and this is well supported by the AFM images (see Figure 5).

In Figure 8b we can see that for bare electrode and first MSA and pLys layers, the diffusion impedance coincides with the Warburg element (slope unity in the Nyquist plots, see inset). Note that the diffusion impedance Z_d in eq 1 reduces to a Warburg element in the limit of vanishing coverage, that is, in the case of a bare electrode. The circuit in Figure 2 reduces then to the traditional Randles circuit. In this limit, the film resistance R_f also vanishes and the two capacitances C_f and C_{dl} merge into a single equivalent one, $C_{eq} = C_{dl} + C_f$.

As more layers are added, the Warburg line splits in three domains. The domain at high (A) and low (C) frequencies are planar semiinfinite-like diffusion regions in the frequency range (described accurately by eqs 4 and 5, respectively). The contribution of nonlinear diffusion due to pinholes is mostly noticed at intermediate frequencies (B). The presence of pinholes is more important for NPs terminated multilayers than for pLys ones, because pLys tends to soften the multilayer structure and thus facilitates the diffusion of the probe ions (lower R_f and θ and higher D_R and r_a) and the incorporation of electroactive species (although this is not so marked because of the partition coefficient $K = 1.23$ is close to unity). NPs terminated multilayers, on the contrary, make the films more compact and oppose a higher resistance to the ionic diffusion, so that the pinholes become the preferential paths for mass transport.

4.4. Electrochemical Characterization Using $[Ru(NH_3)_6]^{3+/2+}$ as Electroactive Species. The presence of Au NPs in the outer layer is favorable for the incorporation of $[Ru(NH_3)_6]^{3+/2+}$ ions. The higher electrochemical reversibility of the CVs, depicted through higher peak currents and smaller peak-to-peak separation (of about 65 mV), is observed when negatively charged Au NPs terminate the film (Figure 9a). The pLys terminated films (Figure 9b) exhibit a larger resistance to charge transfer, as could be expected from the like charge of the electroactive species and the outermost layer, and increasing irreversibility

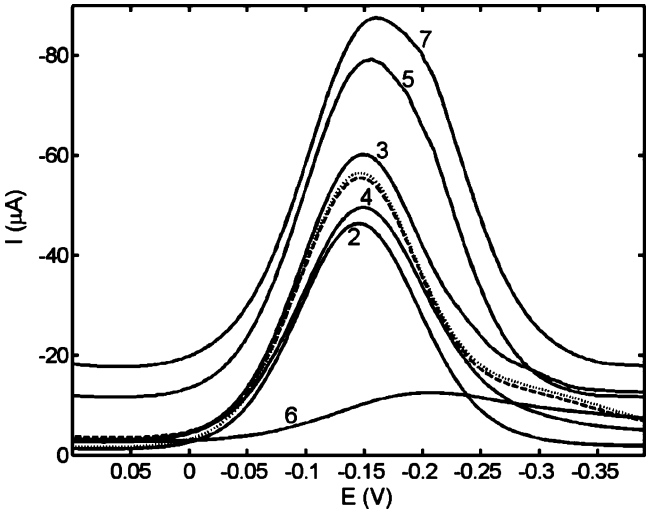

Figure 10. Square-wave voltammograms of the multilayer modified electrode in an aqueous 0.1 M $NaNO_3$ solution containing 1 mM $[Ru(NH_3)_6]^{3+}$ for the numbers of layers indicated. The starting potential was 0.1 V. The results for the bare electrode (dotted curve) and the first MSA layer (dashed curve) are shown for comparison.

with *n* is observed. However, comparison of Figures 6a and 9b proves that the increase in resistance is not so significant in the latter case. In particular, no plateaus are observed in the CVs (at this stage of multilayer growth).

Figure 10 shows the square-wave voltammograms for the reduction of $[Ru(NH_3)_6]^{3+}$. It is interesting to note the current enhancement effect exhibited by the NPs terminated multilayers: the net peak currents are highest when NPs layers are the terminating ones in the multilayer. Compared to the bare gold electrode, the peak currents obtained for NPs terminated multilayers are higher by about 30%. This shows that the presence of Au NPs favors the reduction of $[Ru(NH_3)_6]^{3+}$.

The impedance spectra for $[Ru(NH_3)_6]^{3+}$ are given in Figure 11. For their analysis, it is interesting to note that the diffusion impedance Z_d in eq 1 becomes a Warburg element in the limit of vanishing coverage, that is, in the case of a bare electrode. The circuit in Figure 2 reduces then to the traditional Randles circuit. In this limit, the film resistance R_f also vanishes and the two capacitances C_f and C_{dl} merge into a single equivalent one, $C_{eq} = C_{dl} + C_f$. Indeed, the observed impedance response has vanishing film resistance for *n* odd. This is consistent with a previous finding where a single pLys/NPs bilayer was considered.[30] There, the NPs layer was suggested to behave as a two-dimensional array of randomly distributed nanoelectrodes showing a large electronic overlap with the metal substrate.[30] The behavior observed here for higher *n* with Au NPs terminated multilayers is also consistent with another previous work[34] in which significant communication between NPs of different layers, as well as with neighboring ones in the same plane, was proven by scanning electrochemical microscopy. There are some previous results that have reported also bulk metal conductivity.[53] From our EIS and voltammetry studies we conclude that the main charge transport mechanism for NPs terminated multilayers in the presence of the redox couple $[Ru(NH_3)_6]^{3+/2+}$ is electron transport mediated by the NPs.

Moreover, a current enhancement effect is observed in Figure 10. Because the electroactive species are positively charged, it is plausible to observe a higher current for *n* odd than for *n* even, but the current increases with the number of layers (for NPs terminated films), which suggests that the sensitivity of the electrode is improved by the Au NP layers. Similar behavior was observed for Au NP multilayers on ITO electrodes.[31]

TABLE 2: Parameter Values Used for Fitting the Impedance Data in Figure 11[a]

n	C_f (μF)	R_f (kΩ)	θ	r_a (μm)	D_R
0	0.61 ± 0.01				1.00 ± 0.01
1	1.10 ± 0.01	1.85 ± 0.01			1.00 ± 0.01
		pLys Terminated Multilayers			
2	0.81 ± 0.01	0.50 ± 0.03			0.91 ± 0.01
4	0.81 ± 0.01	0.55 ± 0.03			0.99 ± 0.01
6	0.83 ± 0.01	7.5 ± 0.1	0.39 ± 0.03	4.0 ± 0.8	0.36 ± 0.02
		Au NPs Terminated Multilayers			
3	3.02 ± 0.03				1.00 ± 0.01
5	6.31 ± 0.04				1.00 ± 0.01
7	11.0 ± 0.1				1.00 ± 0.01

[a] Values are given for the 95% confidence bounds of the parameters. The partition coefficient K is unity in all cases.

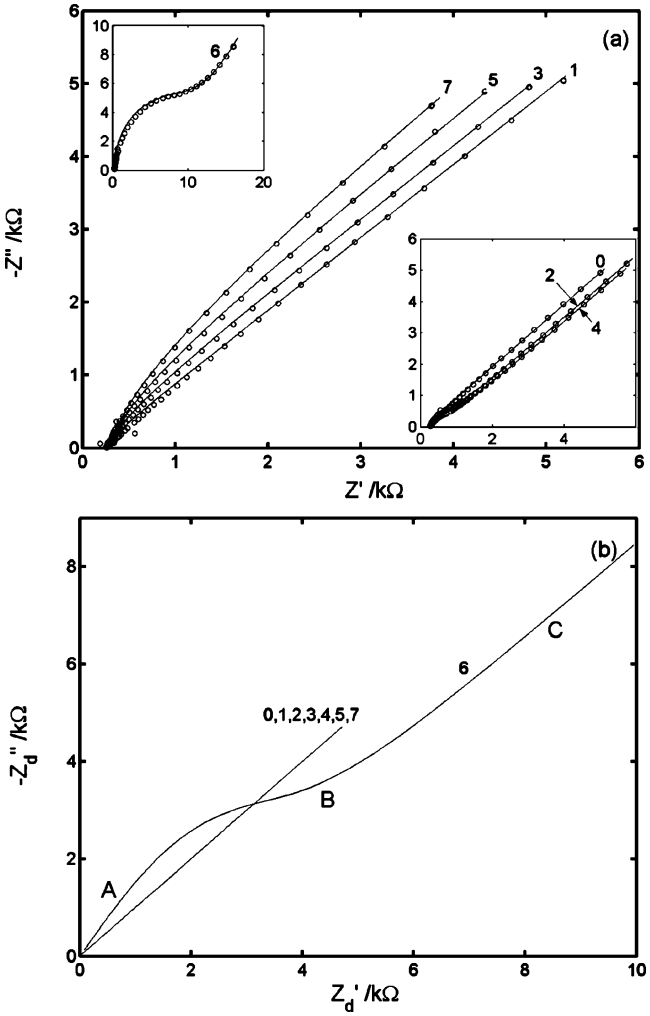

Figure 11. (a) Nyquist diagrams of the multilayer modified electrode in an aqueous 0.1 M $NaNO_3$ solution containing 1 mM $[Ru(NH_3)_6]^{3+}$. The number of layers n is indicated close to the curves. The experimental data are represented by circles, and the solid lines have been calculated from the parameter values in Table 2. (b) Corresponding diffusion impedances Z_d calculated from eq 1.

Remarkably, the only parameter varying with n for NPs terminated multilayers is the capacitance, $C_{eq} = C_{dl} + C_f$ (Table 2). This increase in the capacitance is probably due to both an increase of the film area and changes in the dielectric constant induced by the NPs.[55] At low frequencies the slope of the impedance curves is unity, thus indicating semi-infinite planar diffusion to the film (see Figure 11b). There are no traces of nonlinear diffusion between, and it is therefore to be concluded that the nanoparticles are interconnected both laterally and perpendicularly to the gold electrode due to the large electronic overlap. It is important to note that the impedance decreases at any given frequency with increasing n. This behavior is opposite to the one observed in PEMUs, in which impedance always increases with the number of layers.[18−28]

The importance of the last layer deposited in the multilayer proves again decisive for this system if we consider now the pLys terminated multilayers (see insets in Figure 11). Although for multilayers with two and four layers the trend in the current is to slightly increase with n (and that of impedance to decrease), this behavior suddenly changes for six layers, in which a jump in the impedance is observed. At this regime of the buildup process, the pLys layer binds more effectively to the previous NPs layer (because of the attainment of a more compact structure), and electron transfer through the NPs is precluded. The film resistance jumps about 2 orders of magnitude, and ion transport takes then place through defects. Nonlinear diffusion is observed now at intermediate frequencies, and PEMU-like behavior is regained (see Figure 11b). It is noted that the catalytic effect of the inner NPs is lost even for $n = 2$ and 4 layers because the peak current is lower than for the bare electrode (the impedance being higher).

5. Conclusions

The redox pairs $[Fe(CN)_6]^{3-/4-}$ and $[Ru(NH_3)_6]^{3+/2+}$ have been used as electroactive species to gain insight into the mechanisms of charge transport through pLys/Au NPs multilayers, and a high sensitivity to the charge of the outermost layer has been shown. The CMM, previously considered in PEMUs studies, has allowed us to interpret the experimental results, and the findings can be summarized as follows. When negatively charged $[Fe(CN)_6]^{3-/4-}$ ions are used, the charge is transported by ionic diffusion. For Au NPs terminated multilayers the impedance is high and the permeability low (and decreases with increasing number of layers n), and transport takes place mostly through defects and preferential paths within the multilayer. For pLys terminated multilayers the transport mechanism is also diffusive, but the impedance is much lower (and the permeability much higher), probably due to Donnan inclusion. The important changes in the film impedance after the addition of every new layer are then associated with changes in the film resistance, coverage, radius of the pinholes, and diffusion coefficient. These changes result from the alternate opening and closing of preferential paths for diffusion and from the charge of the outermost layer. Noteworthy, the changes observed for the pLys/Au NPs multilayers are much more pronounced than those in PEMUs.

The conclusions are different when the electroactive species are $[Ru(NH_3)_6]^{3+/2+}$. In this case the NPs terminated multilayers are permeable and yield reversible voltammograms. Quite interestingly, the permeability increases with the number of layers, and the peak currents are higher than for the bare electrode. This feature is attributed to the catalytic effect of the NPs, and work is in progress to exploit it in novel electrochemical sensors. No such current enhancement is observed in pLys terminated multilayers, thus emphasizing again the important role of the outermost layer. These conclusions have been supported through a complete characterization of the multilayers by means of UV−vis absorption spectroscopy, cyclic and square-wave voltammetry, EIS, and AFM. With the latter technique we have proven the existence of defects in the pLys/Au NPs multilayers, which are shown to evolve with the number of layers in consistency with the predictions of the CMM.

Acknowledgment. M.C. thanks Päivi Ahonen and Timo Laaksonen for interesting discussions and technical assistance with TEM images and Peter Eaton for technical assistance with the AFM measurements. V.G.-M. thanks Sergio V. P. Barreira for discussions. Financial support from the European Union under the network SUSANA ("Supramolecular Self-Assembly of Interfacial Nanostructures", Contract HPRN-CT-2002-00185) and from the Ministry of Science and Technology of Spain and FEDER under Project MAT2002-00646 is gratefully acknowledged.

References and Notes

(1) Cao, Y. W. C.; Jin, R. C.; Mirkin, C. A. *Science* **2002**, *297*, 1536.
(2) Niemeyer, C. M. *Angew. Chem., Int. Ed.* **2001**, *40*, 4128.
(3) Heath, J. R.; Kuekes, P. J.; Snider, G. S.; Williams, S. R. *Science* **1998**, *280*, 1716.
(4) Xiao, Y.; Patolsky, F.; Katz, E.; Hainfeld, J. F.; Willner, I. *Science* **2003**, *299*, 1877.
(5) Bethell, D.; Schiffrin, D. J. *Nature* **1996**, *382*, 581.
(6) Lee, J.; Hwang, S.; Lee, H.; Kwak, J. *J. Phys. Chem. B* **2004**, *108*, 5372.
(7) Maxwell, D.; Taylor, M. J.; Nie, S. *J. Am. Chem. Soc.* **2002**, *124*, 9606.
(8) Hicks, J. F.; Seok-Shon, Y.; Murray, R. W. *Langmuir* **2002**, *18*, 2288.
(9) Jiang, C. Y.; Markutsya, S.; Tsukruk, V. V. *Langmuir* **2004**, *20*, 882.
(10) Baum, T.; Bethell, D.; Brust, M.; Schiffrin, D. J. *Langmuir* **1999**, *15*, 866.
(11) Hostetler, M. J.; Green, S. J.; Stokes, J. J.; Murray, R. W. *J. Am. Chem. Soc.* **1996**, *118*, 4212.
(12) Terrill, R. H.; Postlethwaite, T. A.; Murray, R. W. *J. Am. Chem. Soc.* **1995**, *117*, 12543.
(13) Meldrum, F. C.; Kotov, N. A.; Fendler, J. H. *J. Phys. Chem.* **1994**, *98*, 4506.
(14) Dai, J.; Bruening, M. L. *Nano Lett.* **2002**, *2*, 497.
(15) Brust, M.; Bethell, D.; Kiely, C. J.; Shiffrin, D. J. *Langmuir* **1998**, *14*, 5425.
(16) Sarathy, V. K.; Thomas, P. J.; Kulkarni, G. U.; Rao, C. N. R. *J. Phys. Chem.* **1999**, *103*, 399.
(17) *Multilayer Thin Films—Sequential Assembly of Nanocomposite Materials*; Decher, G., Schlenoff, J. B., Eds.; Wiley-VCH: Weinheim, Germany, 2002.
(18) Farhat, T. R.; Schlenoff, J. B. *Langmuir* **2001**, *17*, 1184.
(19) Farhat, T. R.; Schlenoff, J. B. *J. Am. Chem. Soc.* **2003**, *125*, 4627.
(20) Rmaile, H. H.; Farhat, T. R. *J. Phys. Chem. B* **2003**, *107*, 14401.
(21) Krasemann, L.; Tieke, B. *Langmuir* **2000**, *16*, 287.
(22) Antipov, A. A.; Sukhorukov, G. B.; Möhwald, H. *Langmuir* **2003**, *19*, 2444.
(23) Han, S.; Lindholm-Sethson, B. *Electrochim. Acta* **1999**, *45*, 845.
(24) Harris, J. J.; Bruening, M. L. *Langmuir* **2000**, *16*, 2006.
(25) Pardo-Yissar, V.; Katz, E.; Lioubashevski, O.; Willner, I. *Langmuir* **2001**, *17*, 1110.
(26) García-Morales, V.; Silva, T. H.; Moura, C.; Manzanares, J. A.; Silva, F. *J. Electroanal. Chem.* **2004**, *569*, 111.
(27) Barreira, S. V. P.; García-Morales, V.; Pereira, C. M.; Manzanares, J. A.; Silva, F. *J. Phys. Chem. B* **2004**, *108*, 17973.
(28) Silva, T. H.; García-Morales, V.; Moura, C.; Manzanares, J. A.; Silva, F. *Langmuir* **2005**, *21*, 7461.
(29) Markarian, M. Z.; El Harakeh, M.; Halaoui, L. I. *J. Phys. Chem. B* **2005**, *109*, 11616.
(30) Kakkassery, J. J.; Abid, J. P.; Carrara, M.; Fermin, D. J. *Faraday Discuss.* **2004**, *125*, 157.
(31) Yu, A. M.; Liang, Z. J.; Cho, J. H.; Caruso, F. *Nano Lett.* **2003**, *3*, 1203.
(32) Carrara, M.; Kakkassery, J. J.; Abid, J. P.; Fermin, D. J. *Chem. Phys. Chem.* **2004**, *5*, 571.
(33) Cant, N. E.; Zhang, H. L.; Critchley, K.; Mykhalyk, T. A.; Davies, G. R.; Evans, S. D. *J. Phys. Chem. B* **2003**, *107*, 13557.
(34) Ruiz, V.; Liljeroth, P.; Quinn, B. M.; Kontturi, K. *Nano Lett.* **2003**, *3*, 1459.
(35) Murthy, V. S.; Cha, J. N.; Stucky, G. D.; Wong, M. S. *J. Am. Chem. Soc.* **2004**, *126*, 5292.
(36) Hammond, P. T. *Adv. Mater.* **2004**, *16*, 1271.
(37) Geshi, T.; Tokuda, K.; Matsuda, H. *J. Electroanal. Chem.* **1978**, *89*, 247.
(38) Geshi, T.; Tokuda, K.; Matsuda, H. *J. Electroanal. Chem.* **1979**, *101*, 29.
(39) Tokuda, K.; Geshi, T.; Matsuda, H. *J. Electroanal. Chem.* **1979**, *102*, 41.
(40) Amatore, C.; Saveant, J. M.; Tessier, D. *J. Electroanal. Chem.* **1983**, *147*, 39.
(41) Finklea, H. O.; Snider, D. A.; Fedyk, J.; Sabatani, E.; Gafni, Y.; Rubinstein, I. *Langmuir* **1993**, *9*, 3660.
(42) Brookes, B. A.; Davies, T. J.; Fisher, A. C.; Evans, R. G.; Wilkins, S. J.; Yunus, K.; Wadhawan, J. D.; Compton, R. G. *J. Phys. Chem. B* **2003**, *107*, 1616.
(43) Hubrecht, J.; Embrechts, M.; Bogaerts, W. *Electrochim. Acta* **1993**, *38*, 1867.
(44) Ladam, G.; Schaad, P.; Voegel, J. C.; Schaaf, P.; Decher, G.; Cuisinier, F. *Langmuir* **2000**, *16*, 1249.
(45) Picart, C.; Lavalle, Ph.; Hubert, P.; Cuisinier, F. J. G.; Decher, G.; Schaaf, P.; Voegel, J. C. *Langmuir* **2001**, *17*, 7414.
(46) Chen. S.; Kimura, K. *Langmuir* **1999**, *15*, 1075.
(47) Wade, L. G., Jr. *Organic Chemistry*; Prentice Hall: New York, 1987; p 978.
(48) Maya, L.; Stevenson, K. A.; Muralidharan, G.; Thundat, T. G.; Kenik, E. A. *Langmuir* **2002**, *18*, 2392.
(49) Fauth, K.; Kreibig, U.; Schmid, G. *Z. Phys. D* **1989**, *12*, 515.
(50) Duff, D. G.; Baiker, A.; Edwards, P. P. *J. Chem. Soc., Chem. Commun.* **1993**, 96.
(51) Alvarez, M. M.; Khoury, J. T.; Schaaff, T. G.; Shafigullin, M. N.; Vezmar, I.; Whetten, R. L. *J. Phys. Chem. B* **1997**, *101*, 3706.
(52) Goulet, P. J. G.; dos Santos D. S.; Álvarez-Puebla, R. A.; Oliveira, O. N.; Aroca, R. F. *Langmuir* **2005**, *21*, 5576−5581.
(53) Wang, Y.; Liu, Y.; Claus, R. O. *Chem. Phys. Lett.* **1998**, *298*, 315.
(54) Osteryoung, J.; O'Dea, J. J. Square-wave voltammetry. In *Electroanalytical Chemistry*; Bard, A. J., Ed.; Dekker: New York, 1986; Vol. 14, p 209.
(55) Amirudin, A.; Thierry, D. *Prog. Org. Coat.* **1995**, *26*, 1.